Available online at www.sciencedirect.com
SCIENCE DIRECT®
ELSEVIER
Nuclear Instruments and Methods in Physics Research A 526 (2004) 359–375
NUCLEAR INSTRUMENTS & METHODS IN PHYSICS RESEARCH Section A
www.elsevier.com/locate/nima

Computation and inversion of ion spectra for neutron depth profiling of curved surfaces

J. Kenneth Shultis*

Department of Mechanical and Nuclear Engineering, Kansas State University, 137B Ward Hall, Manhattan, KS 66506, USA

Received 8 January 2004; received in revised form 20 February 2004; accepted 24 February 2004

Abstract

Neutron depth profiling (NDP) is a nondestructive technique for determining the concentration of special isotopes within several microns of a sample's surface. Previous NDP analyses, however, have been restricted to samples with plane surfaces. Here samples with curved surfaces are considered. In particular, a method for estimating the energy spectrum of ions emitted from curved surfaces is presented. Also, a robust method for inverting the NDP ion energy spectra is presented that yields accurate concentration profiles for both under- and overdetermined NDP spectra.

Keywords: Neutron depth profiling; Ion energy spectrum; Inversion of spectrum; Deconvolution

1. Introduction

The purpose of neutron depth profiling (NDP) is to determine the concentration (atoms/cm^3) of special isotopes or elements within the first few microns beneath the surface of a sample. Thermal neutrons incident on a sample react with the isotope of interest to produce ions, whose residual energies after escaping through the surface are recorded by an appropriate energy spectrometer. From the measured energy spectrum of the escaping ions, the concentration profile of the isotope can be inferred.

Since the introduction of NDP in 1972 [1], well over 100 papers have been written on the subject (see Ref. [2] for a bibliography) and NDP facilities have been constructed at many research reactors (see Ref. [3] for a review). However, all previous work on NDP has been applied to samples and detectors with plane surfaces. Although most ion detectors do indeed have plane surfaces, there are many objects, in which the concentration profile is sought, whose surface is far from planar. For example, in pressurized water reactors that use soluble boron and lithium compounds for reactivity control, boron and lithium can be precipitated out on the surfaces of the long cylindrical Zircaloy fuel rods to form a thin layer of "crude." One proposed method to investigate such deposits is the use of NDP. However, to apply NDP to such an application, it is necessary to develop analytical models to interpret the measured ion-energy spectrum. In this paper, a model to predict NDP ion-energy spectra from curved surfaces is developed. This model, in turn, can then be used to unfold or invert measured multichannel analyzer

*Corresponding author. Tel.: +1-785-532-5626; fax: +1-785-532-6952.
E-mail address: jks@ksu.edu (J.K. Shultis).

0168-9002/$ - see front matter
doi:10.1016/j.nima.2004.02.028

(MCA) ion-energy spectra to obtain the concentration profiles.

2. NDP ion spectra for surfaces of arbitrary curvature

In this section, a model is presented for estimating the energy spectrum of ions emitted from the surface layers of any sample whose radius of curvature is much greater than the range of the ions in the surface material (typically several microns). Key to this model is the availability of the distribution $g(s,t)$ of path lengths s in the sample for ions produced at depth t (measured along the surface normal) that reach a plane detector of finite size. It is assumed that the concentration of the isotope of interest varies only with t, i.e., at a constant depth there is no variation parallel to the surface. Specifically, let $g(s,t)\,\mathrm{d}s$ be the probability that, an ion born at depth t and reaching the detector, first travels a distance within $\mathrm{d}s$ about s in the sample material before escaping the sample and streaming to the detector.

Ions reaching the detector surface after travelling a path length s in the sample are recorded with a distribution of energies about a *mean* residual energy $\overline{E}(s)$. This spread of energies results from *energy straggling* in the sample and from *detector energy spreading*.

As ions travel through the sample material, they undergo a myriad of stochastic interactions with the ambient atoms losing slightly different amounts of energy, even though they travel exactly the same distance before reaching the surface. In addition, there are numerous small-angle scatters that cause ions to travel slightly different distances in the sample before reaching the surface and, thereby, emerge with a spread of energies. These two effects on the energy spreading are collectively referred to in this paper as *energy straggling*.

The detector system itself further broadens the recorded ion energies as a result of its inherent resolution. Three contributions can be identified: (1) electronic noise of the amplifier chain, (2) intrinsic noise in the detector, caused primarily by leakage currents, and (3) the stochastic variation in energy deposition by the ionizing interactions and stochastic competition with phonon production in the detector material [4,5].

If it is assumed that these energy broadening effects can be adequately described by Gaussian-like behaviors, then the probability of an ion escaping the sample surface with a mean residual energy $\overline{E}(s)$ is recorded by the spectrometer as having an energy in $\mathrm{d}E$ about E is

$$G(E,\overline{E}(s),\sigma(s))\,\mathrm{d}E = \frac{1}{\sqrt{2\pi}\sigma(s)}\exp\left[-\frac{(\overline{E}(s)-E)^2}{2\sigma^2(s)}\right] \tag{1}$$

where $\sigma(s)$ is the standard deviation of all the energy broadening effects for an ion with path length s in the sample. If $\sigma_k(s)$ is the standard deviation of the kth broadening effect, then $\sigma(s) = \sqrt{\sum_k \sigma_k^2(s)}$. The probability an ion born at depth t is recorded with an energy in $\mathrm{d}E$ and E is

$$p(E,t)\,\mathrm{d}E = \left[\int_{s_{\min}(t)}^{s_{\max}(t)} g(s,t)\,G(E,\overline{E}(s),\sigma(s))\,\mathrm{d}s\right]\mathrm{d}E. \tag{2}$$

Here $s_{\min}(t)$ and $s_{\max}(t)$ are the minimum and maximum path lengths, respectively, through the sample material that ions, born at depth t, traverse before reaching the detector. Clearly, these limits must not be greater than the range of the ions in the sample material. If $C(t)\,\mathrm{d}t$ is the concentration of the ion producing isotopes of interest at depth t in the sample, the number of ions produced in the sample within $\mathrm{d}t$ about depth t is

$$n(t)\,\mathrm{d}t = \bar{\sigma}_{\mathrm{ion}}\Phi A_s C(t)\,\mathrm{d}t \equiv \kappa C(t)\,\mathrm{d}t \tag{3}$$

where $\bar{\sigma}_{\mathrm{ion}}$ is the thermal-averaged microscopic cross-section for production of the ion of interest by the isotope of interest, Φ the total thermal neutron fluence in the sample over the measurement time, and A_s the sample surface area irradiated by the incident neutron beam and exposed to the detector. Here $\kappa \equiv \bar{\sigma}_{\mathrm{ion}}\Phi A_s$.

The number of ions born in $\mathrm{d}t$ about t and that are recorded by the MCA with energies in $\mathrm{d}E$ about E (assuming perfect detector efficiency) is, therefore,

$$\mathrm{d}Y(E)\,\mathrm{d}E = n(t)\,\mathrm{d}t\,p(E,t)\,\mathrm{d}E. \tag{4}$$

The number of ions born at all depths and recorded with energies in unit energy about E is thus

$$Y(E) = \int_0^{t_{\max}} \mathrm{d}t\, n(t)p(E,t) = \kappa \int_0^{t_{\max}} \mathrm{d}t\, C(t)p(E,t). \quad (5)$$

The number of these ions recorded by the MCA in energy bin i (with energy boundaries $(E_i - \Delta, E_i + \Delta)$ is

$$Y_i = \int_{E_i-\Delta}^{E_i+\Delta} Y(E)\,\mathrm{d}E = \kappa \int_0^{t_{\max}} \mathrm{d}t\, C(t) \int_{E_i-\Delta}^{E_i+\Delta} p(E,t)\,\mathrm{d}E \quad (6)$$

or

$$Y_i = \int_0^{t_{\max}} \mathrm{d}t\, C(t)R_i(t) \quad (7)$$

where the *channel response function* is defined as

$$R_i(t) \equiv \kappa \int_{E_i-\Delta}^{E_i+\Delta} p(E,t)\,\mathrm{d}E = \int_{s_{\min}(t)}^{s_{\max}(t)} \mathrm{d}s\, g(s,t) \times \int_{E_i-\Delta}^{E_i+\Delta} \mathrm{d}E\, p(E,t)G(E,\overline{E}(s),\sigma(s)) = \int_{s_{\min}(t)}^{s_{\max}(t)} g(s,t)W_i(s)\,\mathrm{d}s, \quad (8)$$

and where the *spread function* is defined as

$$W_i(s) \equiv \int_{E_i-\Delta}^{E_i+\Delta} G(E,\overline{E}(s),\sigma(s))\,\mathrm{d}E = \frac{1}{2}\left[\mathrm{erf}\left(\frac{E_i+\Delta-\overline{E}(s)}{\sqrt{2}\sigma(s)}\right) - \mathrm{erf}\left(\frac{E_i-\Delta-\overline{E}(s)}{\sqrt{2}\sigma(s)}\right)\right]. \quad (9)$$

3. The path-length distribution

The sample surface is assumed to be smooth but arbitrarily curved with a radius of curvature that is much greater than the depths t over which the concentration profile is to be obtained. Further, it is assumed that a ray between where the ion is born and any point on the detector is not tangent to the sample surface. For samples with closed surfaces, such as spheres and cylinders, this latter condition requires collimation or masking of the sample to prevent ions leaving at tangents to the surface from reaching the detector.

Under the above two conditions, it is shown in Appendix A that the ion path length in the sample along the ray between the point where the ion is born at depth t and a point on the detector is proportional the t. This means that the path-length probability distribution $g(s,t_1)$ obtained for depth t_1 can be scaled to obtained the path-length distribution for another depth t_2 as

$$g(s,t_2) = \frac{t_1}{t_2} g(t_1 s/t_2, t_1). \quad (10)$$

3.1. Path-lengths in a cylindrical sample

To illustrate how the path-length distribution is obtained, we consider the case of a cylindrical sample shown in Fig. 1. An ion is emitted from a differential element of area $\mathrm{d}A_s$ with outward normal $\hat{\mathbf{n}}_s$ located at position $\mathbf{r}_s$. The ion travels along a straight line to the detector element $\mathrm{d}A_d$ with outward normal $\hat{\mathbf{n}}_d$ located at $\mathbf{r}_d$. The

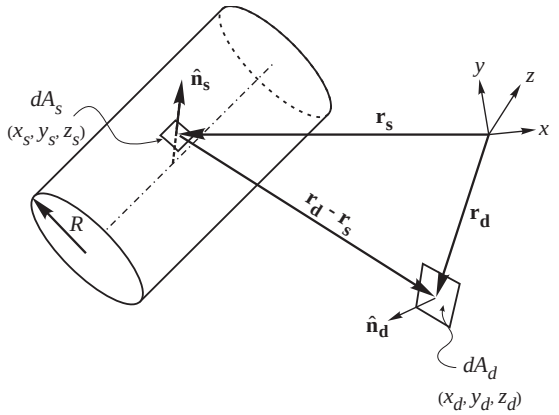

Fig. 1. Geometry for a differential source area $\mathrm{d}A_s$ on the cylindrical sample and a differential detector area $\mathrm{d}A_d$.

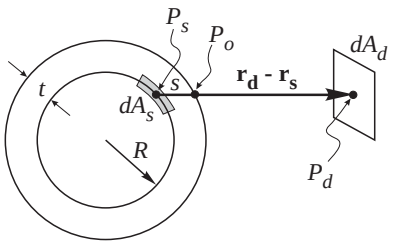

Fig. 2. A ray from an element of the sample dA_s at P_s to an element dA_d at P_d. The path length is the distance from P_s to the point P_o where the ray intersects the cylindrical surface.

path-length s is that portion of the vector $\mathbf{r}_d - \mathbf{r}_s$ inside the sample (see Fig. 2).

Because $t \ll R$, the radius of a sublayer at any depth t (at most several microns) can be taken as the radius R of the cylinder. From Fig. 2, the path length in the sample of an ion born at P_s and headed towards the detector at P_d is the distance from P_s to P_o, the point on the sample surface (of radius $R+t$) from which the ion emerges. The equation of the line through the point P_s to P_d is

$$x = x_s + \alpha d, \quad y = y_s + \beta d, \quad \text{and } z = z_s + \gamma d \quad (11)$$

where $\alpha = x_s - x_d$, $\beta = y_s - y_d$ and $\gamma = z_s - z_d$. Here d is the fractional distance from P_s to P_d at which the point (x, y, z) lies.

To find s, we need the fractional distance from P_s to P_o, i.e., the intersection of the line of Eq. (11) to the cylindrical surface given by

$$x^2 + y^2 = (R+t)^2 \quad (12)$$

where the origin of the coordinate system is assumed to be on the cylinder's axis that is also the z-axis. Substitution of Eq. (11) into Eq. (12) yields

$$(\alpha^2+\beta^2)d^2 + 2(\alpha x_s + \beta y_s)d + [x_s^2 + y_s^2 - (R+t)^2] = 0. \quad (13)$$

The positive real root of Eq. (13) is

$$d = \frac{1}{\alpha^2+\beta^2}\left\{-(\alpha x_s + \beta y_s) + \sqrt{(\alpha x_s + \beta y_s)^2 + (\alpha^2+\beta^2)2Rt}\right\}. \quad (14)$$

As long as $\alpha x_s + \beta y_s \neq 0$ (corresponding to the case that the line $P_s \to P_d$ is tangent to the cylinder of radius R), Eq. (14) may be well approximated by

$$d \simeq \frac{Rt}{(\alpha^2+\beta^2)}. \quad (15)$$

Since the distance from P_s to P_d is $\ell = \sqrt{\alpha^2+\beta^2+\gamma^2}$, the path length an ion travels in the sample is

$$s = \ell d \simeq \frac{\sqrt{\alpha^2+\beta^2+\gamma^2}}{(\alpha^2+\beta^2)} Rt. \quad (16)$$

The negative real root of Eq. (13) corresponds to the fractional distance on the "backside" of the cylindrical surface at which an ion born at depth t escapes the sample along the line through P_s–P_d. It is assumed that the cylindrical sample is sufficiently large (more than tens of micrometers) such that ions born on the backside cannot reach the detector.

3.2. Formulation of the path-length probability distribution

The probability an ion emitted isotropically from dA_s heads towards dA_d (see Fig. 1) is

$$\Pr(dA_s \to dA_d) = \frac{dA_d \cos\theta_d}{4\pi|\mathbf{r}_d - \mathbf{r}_s|^2} \quad (17)$$

where $\cos\theta_d$ is the angle between the vector $\mathbf{r}_s - \mathbf{r}_d$ and the normal $\hat{\mathbf{n}}_d$ to the arbitrarily oriented detector element dA_d, namely

$$\cos\theta_d = \frac{\hat{\mathbf{n}}_d \cdot (\mathbf{r}_s - \mathbf{r}_d)}{|\mathbf{r}_s - \mathbf{r}_d|} \equiv \omega_d. \quad (18)$$

For uniform ion emission per unit area over the surface at depth t of v ions/cm^2, the number of ions reaching the detector after travelling within a unit distance about s in the sample (assuming a straight-line passage through the sample) is

$$\begin{aligned} N(s) &= v \int_{A_s} dA_s \int_{A_d} dA_d \left(\frac{\omega_d}{4\pi|\mathbf{r}_s - \mathbf{r}_d|^2}\right) \times \delta(s - s(\mathbf{r}_s, \mathbf{r}_d, t)) \\ &= v \int_{A_s} dA_s \int_{A_d} dA_d \left(\frac{\hat{\mathbf{n}}_d \cdot (\mathbf{r}_s - \mathbf{r}_d)}{4\pi|\mathbf{r}_s - \mathbf{r}_d|^3}\right) \times \delta(s - s(\mathbf{r}_s, \mathbf{r}_d, t)). \end{aligned} \quad (19)$$

Here δ is the Dirac delta function, and $s(\mathbf{r}_s, \mathbf{r}_d, t)$ is the path length in the sample that an ion born at depth t at $\mathbf{r}_s$ traverses while heading towards point $\mathbf{r}_d$ on the detector surface. For the case of a cylindrical sample, $s(\mathbf{r}_s, \mathbf{r}_d, t)$ is given by Eq. (16). The integration in Eq. (19) is performed over the entire sample area A_s exposed to the detector of area A_d.

Normalization of this quantity to the total number of ions born at depth t, vA_s, gives the probability distribution function that an ion reaches the detector after travelling a unit distance about s in the sample, namely

$$g(s,t) = \begin{cases} N(s)/vA_s, & s_{\min}(t) \leqslant s \leqslant s_{\max}(t) \\ 0, & \text{otherwise.} \end{cases} \tag{20}$$

Here $s_{\min}(t)$ and $s_{\max}(t)$ are the minimum and maximum path-lengths ions travel through the sample material, respectively, before reaching the detector as constrained by any collimation placed around the sample and by the range of the ions in the sample material.

3.2.1. Special case of plane samples

For the case that the sample has a planar surface, the path length depends only on the cosine of the emission angle θ_s and the depth t, namely $s = t/\cos\theta_s \equiv t/\omega_s$ (see Fig. 3). In this case, the path length of Eq. (16) reduces to

$$s = t/\cos\theta_s = t \Big/ \frac{\hat{\mathbf{n}}_s \cdot (\mathbf{r}_d - \mathbf{r}_d)}{|\mathbf{r}_s - \mathbf{r}_d|}. \tag{21}$$

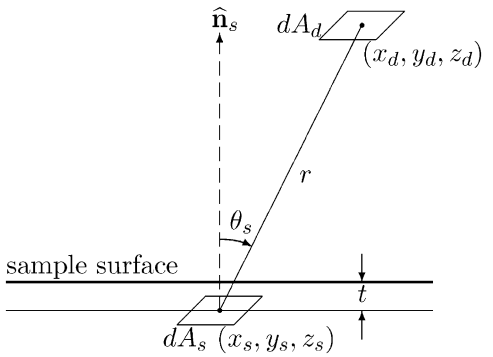

Fig. 3. Geometry for estimating the geometric energy broadening effect in plane geometry. Ions born in $\mathrm{d}A_s$ travel a path length $s = t/\cos\theta_s$ to reach a differential area $\mathrm{d}A_d$ of the detector.

Moreover, in this special case of a planar sample, it is somewhat simpler to calculate the probability distribution of emission angles (or their cosines) $f(\omega_s, t)$ allowed by the finite sizes of the sample and detector. This emission-angle distribution is essentially the same for ions emitted at all depths t in the sample since the sample-detector distance is always much greater than the range of ions ion the sample, i.e., $f(\omega_s, t) \simeq f(\omega_s)$. This is the approach used by Maki et al. [5]. This emission-cosine distribution f and the path-length distribution g are related by $g(s,t)\,\mathrm{d}s = -f(\omega_s)\,\mathrm{d}\omega_s$, where the minus sign indicates that increasing ω_s causes a decrease in the path length s. The path-length distribution can thus be computed from the emission-cosine distribution as

$$g(s,t) = -f(\omega_s)\frac{\mathrm{d}\omega_s}{\mathrm{d}s} = f(t/s)(t/s^2). \tag{22}$$

3.3. Calculation of the path-length distribution

To generate a histogram of the path-length distribution numerically, one calculates

$$G_n(t) \equiv \int_{s_n-\Delta s}^{s_n+\Delta s} g(s,t)\,\mathrm{d}s \simeq 2g(s_n,t)\,\Delta s. \tag{23}$$

This is the probability an ion born at depth t reaches the detector after travelling through the sample with a path length between $s_n - \Delta s$ and $s_n + \Delta s$, where we have assumed an equi-s mesh with bins of width $2\Delta s$.

Substitution of Eq. (20) into Eq. (23) yields

$$\begin{aligned} G_n &= \frac{1}{A_s}\int_{A_s}\mathrm{d}A_s \int_{A_d}\mathrm{d}A_d \left(\frac{\omega_d}{4\pi|\mathbf{r}_s - \mathbf{r}_d|^2}\right) \\ &\quad \times \int_{s_n-\Delta s}^{s_n+\Delta s} \mathrm{d}s\,\delta(s - s(\mathbf{r}_s, \mathbf{r}_d, t)) \\ &= \frac{1}{A_s}\int_{A_s}\mathrm{d}A_s \int_{A_d}\mathrm{d}A_d \left(\frac{\omega_d}{4\pi|\mathbf{r}_s - \mathbf{r}_d|^2}\right) \\ &\quad \times H(s_n, \Delta s, \mathbf{r}_s, \mathbf{r}_d, t)) \end{aligned} \tag{24}$$

where

$$H(s_n, \Delta s, \mathbf{r}_s, \mathbf{r}_d, t)) = \begin{cases} 1, & \text{if } s_n - \Delta s \leqslant s(\mathbf{r}_s, \mathbf{r}_d, t) < s_n + \Delta s \\ 0, & \text{otherwise.} \end{cases} \tag{25}$$

To evaluate Eq. (24), replace the integrals by summations over a contiguous array of small finite-sized pixels such that $dA_s \to \Delta A_s$ and $dA_d \to \Delta A_d$. In this manner, we obtain

$$G_n \simeq \frac{1}{A_s}\sum_{i=1}^{N_s}\Delta A_{is}\sum_{j=1}^{N_d}\Delta A_{jd}\left[\frac{(\omega_d)_{ij}}{4\pi r_{ij}^2}\right] \times H(s_n, \Delta s, \mathbf{r}_i, \mathbf{r}_j, t)) \quad (26)$$

where ΔA_{is} is the ith source pixel (one of N_s), ΔA_{jd} is the jth detector pixel (one of N_d), and r_{ij} is the distance between the centers of source pixel i and detector pixel j.

3.4. Example path-length distributions

Figure 4 illustrates the above methodology for a cylindrical sample with a 0.514-cm radius and 2-cm length. The detector is a 1-cm × 1-cm square parallel to and 10 cm from the sample axis whose center is opposite the center of the sample. The sample is masked or collimated so that only ions emitted within polar angles between $\pm 70^\circ$ from the ray between the sample and detector centers are allowed to escape the sample.

In Fig. 4 the circles are values of the path-length distribution $g(s_n, t)$ obtained from Eqs. (23) and (26) for several depths t. The continuous curve in Fig. 4 through the $t = 1$ μm values is an empirical fit to these values obtained with TableCurve [6]. The continuous curves for other depths are the empirical fit for $t = 1$ μm scaled by Eq. (10). The agreement between the numerically evaluated values and the scaled empirical distribution clearly demonstrates the validity of the scaling property of $g(s, t)$. Thus, instead of having to laboriously compute $g(s, t)$ for all depths when constructing or unfolding an MCA ion-energy spectrum, one needs to have $g(s, t)$ evaluated at only a single depth and then scale it to other depths.

In Fig. 5 the path-length distribution of the cylindrical sample considered in Fig. 4 is compared to that of a planar sample with the same exposed surface area (i.e., the exposed cylindrical area is flattened). Both samples are at the same distance from the detector and ions are produced at a depth $t = 1$ μm. Notice, the planar sample has a very limited range of different path lengths and thus, for this geometry, produces small geometric

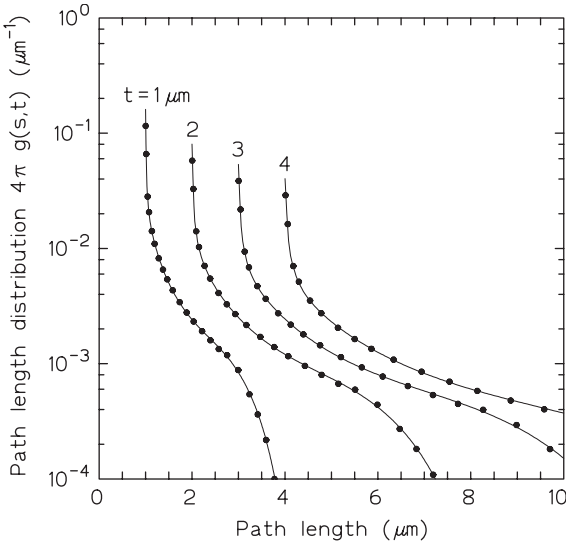

Fig. 4. Path-length distributions $g(s, t)$ for a cylindrical sample. Values of $g(s, t)$ computed with Eqs. (23) and (26) are shown by the circles. The continuous curve through the $t = 1$ μm is an empirical fit, and the other continuous curves were obtained by scaling the $t = 1$ μm curve using Eq. (10).

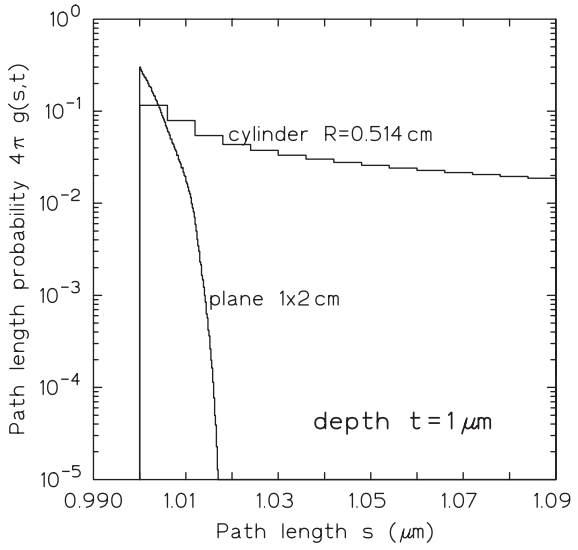

Fig. 5. A comparison of the path-length distributions for cylindrical and planar samples. Both samples have the same exposed surface area (2 cm^2) and are at the same distance from a 1 × 1 cm detector plane. The ions are born at $t = 1$ μm depth in both samples. The cylindrical sample is that considered in Fig. 4.

broadening in the MCA energy deposition spectrum. By contrast, the cylindrical sample displays large geometry broadening (distortion) effects (usually much larger than those caused by ion energy straggling and the detector resolution).

4. Numerical evaluation of the ion energy-deposition spectrum

It is important to be able to compute the expected MCA ion-energy spectrum for a given concentration profile both to interpret better the structure in measured NDP spectra and also to test the robustness of various deconvolution or unfolding schemes used to extract the concentration profiles from the NDP spectra. In this section, we present an algorithm for simulating an NDP spectrum for arbitrary profiles in curved surfaces.

4.1. Discretization of the concentration profile

The expected number of counts in channel n of the MCA spectrum is given by Eq. (7). This integral can be approximated by an appropriate weighted sum of concentrations at discrete depths in the sample by using some quadrature approximation for the integral. Suppose the concentration at M equispaced depths t_j are given such that $t_1 = 0$ and $t_M = t_{\max}$, the depth beyond which an ion cannot escape the sample. The concentration at depth t_j is denoted by $c_j \equiv C(t_j)$. With this discrete spatial grid, Eq. (7) is decomposed into a sum of integrals over the subintervals as

$$Y_i = \int_0^{t_{\max}} \mathrm{d}t\, R_i(t)C(t) = \sum_{j=1}^{M-1} \int_{t_j}^{t_{j+1}} \mathrm{d}t\, R_i(t)C(t). \tag{27}$$

Each integral in Eq. (27) is then evaluated by numerical quadrature to express the integrals in term of the c_j. The resulting linear equations can be written as

$$Y_i = \sum_{j=1}^{M} R_{ij}c_j, \quad i = 1, \ldots, N \tag{28}$$

or, in matrix notation, as $\mathbf{Y} = \mathbf{R} \cdot \mathbf{c}$. This result represents N equations in the M unknowns $\{c_j\}$. Here, the $N \times M$ response matrix $\mathbf{R}$ depends on the numerical quadrature approximation selected to evaluate Eq. (27). For example, suppose $C(t)$ in each of the subintervals is approximated by the average of its end point values. Thus Eq. (27) becomes

$$\begin{aligned} Y_i &\simeq \sum_{j=1}^{M-1} \frac{c_{j+1} + c_j}{2} \int_{t_j}^{t_{j+1}} R_i(t)\,\mathrm{d}x \\ &= \sum_{j=1}^{M-1} \frac{c_{j+1} + c_j}{2} Q_{i,j} \\ &\equiv \sum_{j=1}^{M} R_{ij}c_j, \end{aligned} \tag{29}$$

where the elements of the $\mathbf{R}$ matrix are given by

$$R_{ij} = \frac{1}{2}\begin{cases} Q_{i,1}, & j = 1 \\ Q_{i,j-1} + Q_{i,j}, & j = 2, \ldots, M-1 \\ Q_{i,M-1}, & j = M \end{cases} \tag{30}$$

and

$$Q_{i,j} \equiv \int_{t_j}^{t_{j+1}} R_i(t)\,\mathrm{d}t. \tag{31}$$

The evaluation of $Q_{i,j}$ generally must be performed numerically.

Many other more accurate schemes can be used to approximate the integrals in Eq. (27) [7–9]; however, for the generation of NDP energy spectra, the approximation of Eq. (29) has been shown to be adequate.

4.2. Examples of NDP Ion energy spectra

As discussed in Section 2, an ion leaving the sample surface after travelling a fixed path length s in the sample can be recorded with a spread of energies by the detector system as a result of energy straggling and detector resolution effects. These effects must be quantified before the MCA ion-energy spectrum can be evaluated. Specifically, $\sigma(s)$ in Eq. (1) must be known for a given path length s and sample material. This quantity has two contributions: energy straggling as the ions penetrate the sample, and detector energy broadening from noise and stochastic mechanisms in the detector system.

4.2.1. Energy straggling

To determine the standard deviation of energy straggling $\sigma_{\text{strag}}(s)$, the Monte Carlo ion code TRIM [10] was used to find the standard deviation of initially monoenergetic, normally incident ions that penetrate a slab of the sample material and of thickness s. The results for different slab thicknesses were then fit to an empirical equation to allow efficient calculation of $\sigma_{\text{strag}}(s)$ [7].

4.2.2. Detector energy broadening

For an NDP detector system there are two energy-broadening effects (1) system noise (σ_{noise}) and (2) stochastic variation of the amount of ionization produced by an ion in the detector crystal (σ_{ion}). The overall variance of the detector energy broadening is thus $\sigma^2_{\text{det}} = \sigma^2_{\text{noise}} + \sigma^2_{\text{ion}}$.

The presence of noise in the detector and the amplifier chain perturbs the pulse amplitudes produced by the detector crystal, thereby, leading to a broadening of the recorded energy spectrum. The amount of the energy broadening is usually the same for all ion energies, i.e., $\sigma_{\text{noise}} \simeq$ constant. On the other hand, the stochastic competition between phonon production and ionization by ions in the detector crystal produces different numbers of ionizing events for incident ions of the same initial energy. Because the detector pulse amplitude is directly proportional to the number of ionization events caused by the incident ion, the detector produces different pulse amplitudes leading to an apparent spread of ion energies. The variance σ^2_{ion} of this stochastic ionization effect depends on the energy and charge of the ion as well as the detector material. For most solid state detectors there is negligible phonon production produced by ions of the hydrogen isotopes, and hence $\sigma_{\text{ion}} \simeq$ constant [5]. For ions with a charge greater than one, σ_{ion} generally cannot be neglected and is usually a function of the incident ion energy [5].

To determine the total detector system's energy broadening, $\sigma^2_{\text{det}} = \sigma^2_{\text{noise}} + \sigma^2_{\text{ion}}$, one generally must measure it by recording the MCA spectrum of monoenergetic ions of different energies. Based on NDP spectra taken at Kansas State University's NDP system [7], a typical value of $\sigma_{\text{det}} =$ 0.019 MeV is used in the following examples.

4.2.3. Example spectra

The isotope ^{10}B is readily detected by NDP because of its large thermal-neutron cross-section (3840 b at 0.00253 eV) for the $^{10}\text{B}(\text{n},\alpha)^7\text{Li}$ reaction. Two distinct energies of α and ^{7}Li ions are produced since the ^{7}Li nucleus is produced either in the ground state or in a 0.4776-MeV excited state as shown below.

$$ {}^1_0\text{n} + {}^{10}_5\text{B} \rightarrow \begin{cases} {}^7_3\text{Li}^* + {}^4_2\text{He} & (93.7\%) \\ {}^7_3\text{Li} + {}^4_2\text{He} & (6.3\%). \end{cases} $$

Alpha particles are produced with the two energies 1.7762 MeV (α_1) and 1.4721 MeV (α_2). The corresponding lithium ions have energies 1.0133 MeV (Li_1) and 0.8398 MeV (Li_2).

In Fig. 6, a calculated 256-channel MCA ion energy-deposition spectrum is shown for NIST's SRM-2137 ^{10}B implanted sample. The detector is a 1×1 cm plane parallel to the sample plane whose center is 10 cm from the center of the sample. The ^{10}B profile for this sample is shown in the inset of Fig. 6. This example is designed to show clearly the contributions to the spectrum from the four

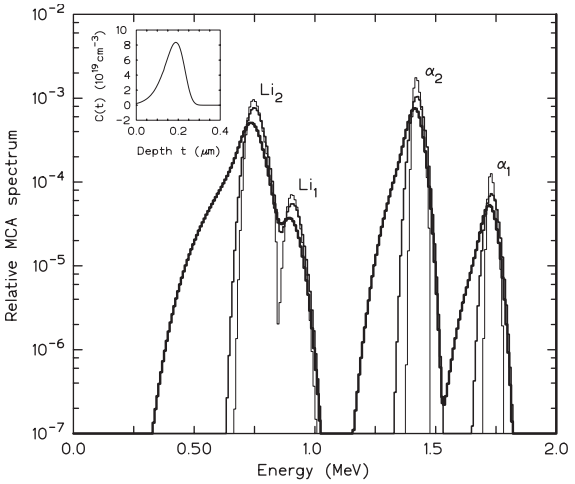

Fig. 6. The predicted MCA energy-deposition spectrum for the NIST SRM-2137 ^{10}B implanted sample. The light line is the spectrum with only energy straggling used. The medium weight line also includes the detector resolution. The heavy line adds geometric energy broadening to the other broadening effects based on the sample being deformed into a cylinder of radius $R = 0.512$ cm.

different energy ions produce in the ^{10}B $(n,\alpha)^7Li$ reaction.

The spectrum with energy straggling was calculated from Eq. (28) using the interval average approximation of Eqs. (29)–(31) with $M = 65$ equispaced t_j between $t = 0$ and 0.320 μm (the values at which NIST tabulates the ^{10}B concentration). For this example, energy straggling is negligible since all the ^{10}B is within 0.32 μm of the sample surface. The two lightest weight lines in Fig. 6 both neglect geometric energy broadening. The heavy line in Fig. 6 is the spectrum with geometric energy broadening added for the (hypothetical) case that the sample is deformed into a cylinder with radius $R = 0.514$ cm collimated to an axial length of 2 cm and to polar angles of $\pm 70^\circ$ from the line joining the sample and detector centers.

Another possible NDP profile problem is to analyze a sample with a constant ^{10}B concentration throughout the sample or from the surface to some specified depth. Figs. 7 and 8 show several such spectra from a cylindrical samples with radius $R = 0.514$ cm, collimated to an axial length of 2 cm and to polar angles of $\pm 70^\circ$ from the line joining the sample and detector centers. The detector is a 1×1 cm plane parallel to the cylinder axis and opposite its center. In Fig. 8, the contributions by the individual ions (light lines) to the total spectrum (heavy line) are also shown.

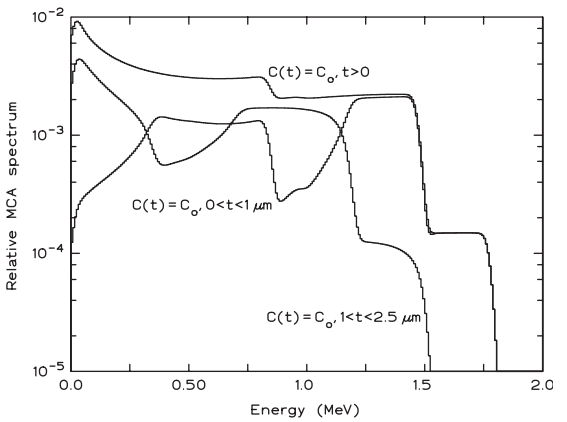

Fig. 7. Calculated MCA energy-deposition spectra for cylindrical samples for various (step-wise) ^{10}B profiles. All energy-broadening effects are included.

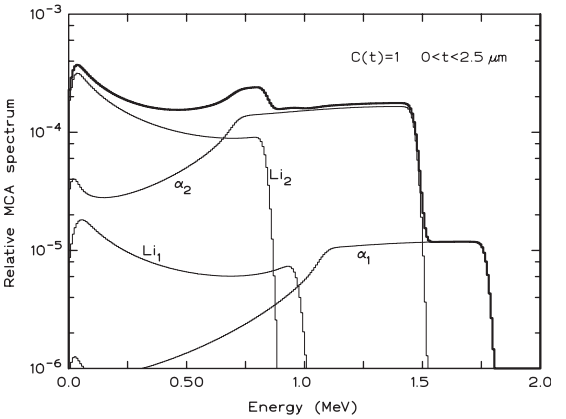

Fig. 8. The MCA energy-deposition spectrum (heavy line) for a cylindrical sample with a constant ^{10}B concentration in the top 2.5 μm layer. The contributions from the four ions are shown by the light lines.

5. The unfolding or inverse problem

In the inverse problem, one attempts to determine from Eq. (7) the concentration profile $C(t)$ given the counts Y_n in each channel of the MCA energy spectrum (or a portion of the spectrum). Most unfolding schemes begin by replacing the Fredholm integral equation of Eq. (7) by a set of N algebraic equations, namely Eq. (28) in M unknown concentration $c_j \equiv C(t_j)$. The inversion of Eq. (28) generally has no unique solution since the number of unknowns M (the c_j) is most likely different from the number N of measured data (the Y_i). If $M < N$ (more equations than unknowns), the problem is overdetermined and generally no solution exists. By contrast, if $M > N$ (more unknowns than equations), there is an infinity of solutions because the solution space (of dimension M) has an $(M - N)$ dimensional degeneracy, i.e., any $(M - N)$ components of $\mathbf{c}$ can be specified arbitrarily and still have Eq. (28) satisfied. This underdetermined case is typical of an NDP spectrum that is concentrated in only a few MCA channels. For NDP spectra from curved surfaces and with the ion-producing isotope distributed over several microns from the surface, the spectrum is typically spread over many channels and often $M > N$, an overdetermined system of equations.

5.1. Review of unfolding techniques for the NDP problem

Several different approaches have been applied to estimate the concentration profile $C(t)$, or the $c_j \equiv C(t_j)$, from the measured MCA channel counts Y_i. Reviewed below are the principal techniques that have been applied to the NDP problem.

5.1.1. Direct methods

In this approach one attempts to describe the concentration profile by some known function $f(t;\boldsymbol{\xi})$ with M parameters ξ_i. Once a concentration model has been selected, a predicted MCA spectrum $\hat{Y}_i, i = 1, \ldots, N$ can be computed from Eq. (7) with $C(t)$ replaced by the model $f(t;\boldsymbol{\xi})$. The "best" values for the model parameters $\boldsymbol{\xi}$ are then obtained by minimizing the disagreement between the measured data and the predicted data. This is often done by minimizing the statistic $\chi^2 = \sum_{i=1}^{N} (Y_i - \hat{Y}_i)^2$ [11]. The direct approach often produces erratic results when there is significant noise in the data or if there is a large number of parameters to be estimated.

5.1.2. Iterative methods

Several iterative techniques have been used for unfolding MCA energy spectral data. Many are ad hoc schemes whose mathematical properties, such as convergence, are not well established. Nevertheless, they often produce useful results, especially if the concentration profile is a slowly varying function of t. A simple iterative scheme proposed long ago by Cittert [12] was used for NDP analysis by Maki et al. [5]. Critical to the success of this procedure is that both the data Y_i and the concentration profile be smooth and slowly varying.

5.1.3. Fourier transform methods

In Eq. (28), the response matrix elements R_{ij} are narrowly peaked around $i \simeq j$, i.e., R_{ij} is large when the residual energy from depth j is near the MCA channel energy E_i. This is particularly true when there is negligible geometric energy broadening. In this case, Eq. (28) can be viewed as a discrete convolution of a signal $C(t)$ with a narrowly peaked response function. Using the convolution theorem for Fourier transforms [9], the discrete Fourier transform of the c_j can be obtained in terms of the discrete Fourier transforms of Y_i and R_{ij}. An inverse Fourier transform then gives estimates of the c_j. The difficulty with Fourier transform techniques is that spurious features are often added to the unfolded profile as a result of aliasing errors produced by the relatively small amount of discrete data in the MCA spectrum.

5.1.4. Least-squares: overdetermined set of equations

For the case in which there are more data than unknowns, the usual procedure is to seek a solution vector $\mathbf{c}$ that minimizes the difference between the data $\mathbf{Y}$ and the MCA spectrum predicted by the NDP model. This difference between a model and measured data is often quantified by the χ^2 statistic, namely,

$$\chi^2 = \sum_{i=1}^{N} \sum_{j=1}^{M} \left[Y_i - \sum_{k=1}^{M} R_{ik} c_k \right] S_{ij}^{-1} \left[Y_j - \sum_{k=1}^{M} R_{jk} c_k \right] \simeq \sum_{i=1}^{N} \frac{1}{\sigma_i^2} \left[Y_i - \sum_{k=1}^{M} R_{ik} c_k \right]^2 = |\mathbf{A} \cdot \mathbf{c} - \mathbf{b}|^2. \quad (32)$$

Here $S_{ij} = \mathrm{Covar}[n_i, n_j]$ are the elements of the covariance matrix. The approximate equality in the above result holds if we can neglect the off-diagonal covariance terms, with $\sigma_i^2 = \mathrm{Covar}[n_i, n_i]$. The matrix $\mathbf{A}$ has elements $A_{ij} = R_{ij}/\sigma_i$ and the vector $\mathbf{b}$ has elements $b_i = Y_i/\sigma_i$. For the counting data of an MCA spectrum, the estimate of σ_i is $\sqrt{Y_i}$ provided Y_i is sufficiently large (namely, $Y_i \gtrsim 20$).

For this overdetermined problem, the *least-squares solution* is obtained with the $\{c_j\}$ that minimize χ^2. At this minimum $\partial\chi^2/\partial c_k = 0$. Differentiating Eq. (32) with respect to c_k and setting the result to zero gives the so-called *normal equations*

$$\sum_{j=1}^{M} \alpha_{kj} c_j = \beta_k, \quad k = 1, \ldots, M \quad (33)$$

where

$$\alpha_{kj} \equiv \sum_{i=1}^{N} \frac{R_{ij}R_{ik}}{\sigma_i^2} \quad \text{and} \quad \beta_k \equiv \sum_{i=1}^{N} \frac{Y_i R_{ik}}{\sigma_i^2}. \tag{34}$$

The solution of these M linear equations in the M c_j unknowns is very susceptible to numerical roundoff errors and often the solution $\mathbf{u}$ obtained with, say, Gauss elimination is often meaningless with adjacent components oscillating between enormous positive and negative values. The reason for this is that the normal equations are often nearly singular because different combinations of the R_{ij} response matrix elements often fit the data equally well (or equally poorly). Consequently, the α matrix, unable to distinguish between nearly equal combinations, becomes close to singular. To avoid such spurious solutions of the normal equations, a different approach to finding the minimum of χ^2 should be used. This approach is to perform the minimization using the *singular value decomposition* (SVD) technique [9]. However, even with this approach small spurious oscillations are often encountered [7].

5.1.5. Regularization: under-determined set of equations

Minimization of the positive functional $\mathscr{A}[\mathbf{c}] \equiv \chi^2 = |\mathbf{A}\cdot\mathbf{c} - \mathbf{b}|^2$ for a matrix $\mathbf{A}$ that is degenerate, i.e., has fewer rows than columns, will not give a unique solution for $\mathbf{c}$. To obtain a unique solution, additional constraints must be imposed on the minimization problem. For example, if any non degenerate strictly convex functional $\mathscr{B}[\mathbf{c}]$, for example $\mathbf{c}^{\mathrm{T}}\cdot H\cdot\mathbf{c}$, is added, then the minimization of $\mathscr{A}[\mathbf{c}] + \lambda\mathscr{B}[\mathbf{c}]$ *will* produce a unique solution $\mathbf{c}$ [9]. The addition of the term $\lambda\mathscr{B}[\mathbf{c}]$ is said to "regularize" the minimization problem, i.e., to produce a unique solution.

Thus in the inverse problem, to obtain a unique solution for $\mathbf{u}$, one solves the following minimization problem

$$\text{minimize}: \quad \mathscr{A}[\mathbf{c}] + \lambda\mathscr{B}[\mathbf{c}]. \tag{35}$$

This is the central principle of inversion theory. As the Lagrange multiplier λ varies from 0 to ∞, the unique solution $\mathbf{c}$ varies from one minimizing $\mathscr{A}[\mathbf{c}]$ to one minimizing $\mathscr{B}[\mathbf{c}]$. However, because of the finite precision of numbers in computers, if λ is made too small, the effect of the regularization term is lost in the roundoff and numerical instabilities arise. For simulated NDP data obtained by accurate numerical integration of Eq. (27), the most accurate inversion will be obtained with λ made as small as possible, but still large enough to avoid numerical instabilities in the minimization algorithm.

The many apparently different regularization approaches used for inversion problems all involve minimizing the functional of Eq. (35) with the choice for $\mathscr{A}[\mathbf{c}]$ and $\mathscr{B}[\mathbf{c}]$ dependent on the problem and the inversion philosophy. In this study the *linear regularization* method is used to unfold NDP energy-deposition spectra that contain large amounts of geometric energy broadening.

5.2. The linear regularization (LR) method

The linear regularization method goes by many names, for example, Tikhonov–Miller regularization [13–16], the Phillips–Twomey method [17,18], the constrained linear inversion method [19], and the method of regularization [20]. As with any method that has evolved from many different disciplines, the notation and ideas in the many seminal works are often quite different.

In the linear regularization approach, the functional $\mathscr{A}[\mathbf{c}]$ of Eq. (35) is taken as the χ^2 of Eq. (32), i.e., $\mathscr{A}[\mathbf{c}] = |\mathbf{A}\cdot\mathbf{c} - \mathbf{b}|^2$, and the functional $\mathscr{B}[\mathbf{c}]$ is chosen as some measure of the smoothness of $C(t)$, which is derived from first or higher derivatives of $C(t)$. In particular, the linear regularization method requires that $\mathscr{B}[\mathbf{c}] = \mathbf{c}^{\mathrm{T}}\cdot\mathbf{H}\cdot\mathbf{c}$, where $\mathbf{H}$ is some appropriate symmetric smoothing matrix. The inversion solution is thus determined by the following minimization problem:

$$\begin{aligned}\text{minimize}: \quad & \mathscr{A}[\mathbf{c}] + \lambda\mathscr{B}[\mathbf{c}] \\ & = |\mathbf{A}\cdot\mathbf{c} - \mathbf{b}|^2 + \lambda\mathbf{c}^{\mathrm{T}}\cdot\mathbf{H}\cdot\mathbf{c}.\end{aligned} \tag{36}$$

The matrix $\mathbf{H}$ is obtained by making some a priori assumption about the nature of the concentration profile $C(t)$. Two example *smoothing* matrices are presented in Section 5.2.1 below.

To obtain the minimum of the functional of Eq. (36) and find $\mathbf{c}$, we write Eq. (36) in its component form as

$$\mathscr{F}[\mathbf{c}] \equiv \mathscr{A}[\mathbf{c}] + \lambda\mathscr{B}[\mathbf{c}] = \sum_{i=1}^{N}\left[\sum_{j=1}^{M} A_{ij}c_j - b_i\right]^2 + \lambda\sum_{i=1}^{M} c_i \sum_{j=1}^{M} H_{ij}c_j. \tag{37}$$

The values of c_j that minimize this functional are the solutions of the M *normal equations* obtain by setting the derivative of $\mathscr{F}[\mathbf{c}]$ with respect to c_j to zero. Differentiation of Eq. (37) with respect to c_j, setting the result to zero, and use of the symmetry property of $\mathbf{H}$ gives

$$\sum_{j=1}^{M}\left\{\left(\sum_{i=1}^{N} A_{ik}A_{ij}\right) + \lambda H_{kj}\right\}c_j = \sum_{i=1}^{M} A_{ik}b_i, \quad k = 1, \ldots, M \tag{38}$$

or, in matrix form,

$$(\mathbf{A}^{\mathrm{T}}\cdot\mathbf{A} + \lambda\mathbf{H})\cdot\mathbf{c} = \mathbf{A}^{\mathrm{T}}\cdot\mathbf{b}. \tag{39}$$

This set of M linear algebraic equations is readily solved for $\mathbf{c}$ using standard techniques such as the lower-upper (LU) decomposition method or the singular value decomposition (SVD) method [9]. Although developed for underdetermined problems, the LR method will be seen to also work very well for overdetermined NDP inversions.

5.2.1. Smoothing matrices

The construction of the $M \times M$ square matrix $\mathbf{H} = \mathbf{B}^{\mathbf{T}}\cdot\mathbf{B}$ depends on the a priori smoothness criterion chosen. For example, if a linear function is thought to be a good approximation for $C(t)$ then, with forward finite differences, one should minimize

$$\mathscr{B}[\mathbf{c}] \propto \int_0^{t_{\max}} [C''(t)]^2\,\mathrm{d}t \propto \sum_{j=1}^{M-2}[-c_j + 2c_{j+1} - c_{j+2}]^2 \tag{40}$$

so that $(M-2)\times M$ $\mathbf{B}$ matrix is

$$\mathbf{B} = \begin{pmatrix} -1 & 2 & -1 & 0 & 0 & 0 & 0 & \ldots & 0 \\ 0 & -1 & 2 & -1 & 0 & 0 & 0 & \ldots & 0 \\ \vdots & & & & \ddots & & & & \vdots \\ 0 & \ldots & 0 & 0 & 0 & -1 & 2 & -1 & 0 \\ 0 & \ldots & 0 & 0 & 0 & 0 & -1 & 2 & -1 \end{pmatrix}. \tag{41}$$

If one believes a quadratic function is a good approximation for $C(t)$, then one should minimize (again with forward finite differences)

$$\mathscr{B}[\mathbf{c}] \propto \int_0^{t_{\max}} [C'''(t)]^2\,\mathrm{d}t \propto \sum_{j=1}^{M-3}[-c_j + 3c_{j+1} - 3c_{j+2} + c_{j+3}]^2 \tag{42}$$

so that the $(M-3)\times M$ $\mathbf{B}$ matrix becomes

$$\mathbf{B} = \begin{pmatrix} -1 & 3 & -3 & 1 & 0 & 0 & 0 & \ldots & 0 \\ 0 & -1 & 3 & -3 & 1 & 0 & 0 & \ldots & 0 \\ \vdots & & & & \ddots & & & & \vdots \\ 0 & \ldots & 0 & 0 & -1 & 3 & -3 & 1 & 0 \\ 0 & \ldots & 0 & 0 & 0 & -1 & 3 & -3 & 1 \end{pmatrix}. \tag{43}$$

Other higher-order and different differencing schemes can be used as well [8,9]; however, these two smoothing matrices have been found to work well for the NDP inversion problem.

5.2.2. Examples of unfolded concentration profiles

The estimated spectrum shown in Fig. 6 is an ideal case for testing the capabilities of LR inversion technique since the contributions from the four different ions are clearly distinguished. In particular, the spectrum component for the 1.47-MeV alpha particle (α_2) was used. In Fig. 9 unfolded ^{10}B concentration profiles are shown by the thin lines for various values of the Lagrange multiplier λ. The actual profile is shown by the heavy dashed line.

In this example, the unfolded profiles are shown as spline fits through the concentrations estimates at 30 equispaced depths. A total of 80 channels of data was used (shown in the inset to Fig. 6) so that for this example the unfolding problems involves an overdetermined set of equations. The

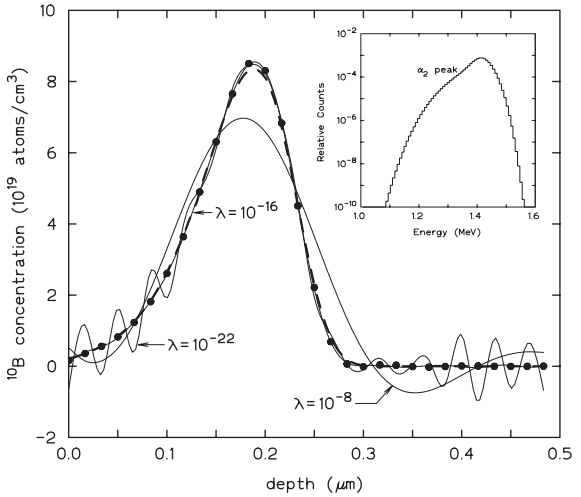

Fig. 9. Unfolded concentration profiles (light lines) using linear regularization with quadratic smoothing. The actual profile is shown as the heavy dashed line. The 80 channels of the simulated MCA energy spectrum for the α_2 ion that were used for the unfolding are shown in the inset. The profile was estimated at $M = 30$ points (circles for the case of $\lambda = 10^{-16}$).

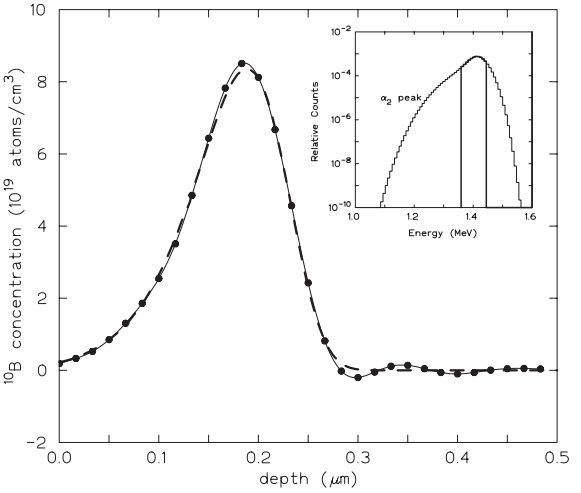

Fig. 10. Unfolded concentration profile (solid line and circles) using linear regularization with linear smoothing for $\lambda = 10^{-18}$. The actual profile used to generate the MCA spectrum is shown by the heavy dashed line. The 11 channels of the simulated MCA energy spectrum for the α_2 ion that were used are shown by the dark histogram in the inset. The profile was estimated at $M = 30$ points (the circles).

λ parameter in the unfolding determines the relative importance of the unfolded profile to minimize the χ^2 statistic (agreement with the spectral data) versus satisfying the smoothing constraint. As seen from Eq. (36), as λ becomes small, less emphasis is placed on the smoothing regularization term.

However, if λ becomes too small, the smoothing term becomes lost in the roundoff of the computer calculations and spurious oscillations appear in the unfolded profile as a result of the ill-conditioned nature of minimizing the χ^2 statistic for the least-squares solution of an overdetermined system, the solution that would be obtained if λ were exactly zero. Such spurious oscillations as seen in Fig. 9 for the profiles obtained with $\lambda = 10^{-22}$. By contrast, if λ becomes too large, inordinate emphasis is placed on achieving a smooth solution and the unfolded profile will becomes flattened and exhibit unrealistic slow oscillations. This is seen in Fig. 9 for the case of $\lambda = 10^{-8}$. For values of λ between these two extremes, quite realistic results are achieved.

The results of Fig. 9 are for an overdetermined unfolding problem. The utility of the LR method, however, is that it is designed for an underdetermined unfolding problem. In Fig. 10 the optimum (λ chosen to give the best agreement with the actual profile) unfolded profile using only the 11 peak channels in the MCA ion energy-deposition spectrum. In this case, the ^{10}B profile was again estimated at 30 equispaced depths from 0 to 0.5 μm (shown as the circles in the figure). Almost identical unfolded profiles are obtained λ between 10^{-14} to 10^{-20} and hence are not plotted. In this example, the 11 MCA channel responses (between mid-point energies 1.363 and 1.441 MeV) are relatively insensitive to ions emitted at depths below since most of the α_2 ions emitted at depths between 0.35 and 0.5 μm will have longer path lengths in the substrate and hence emerge with energies below these 11 MCA channels. Thus, it is not surprising that the zero concentration levels for $t > 0.3$ μm is not quite so well defined in this example as in the previous one which used the lower energy channels.

Step discontinuities. Although the LR method appears to be very robust because it can be applied to both over- and underdetermined problems, it is, nevertheless, based on the premise that the

concentration profile varies smoothly with depth. Consequently, an MCA energy-deposition spectrum obtained from a sample whose ^{10}B concentration profile exhibits sharp discontinuities can be expected to present a severe challenge to the LR unfolding method. Such spectra are shown in Figs. 7 and 8.

To test the capabilities of the LR method for such cases, the α_2 component of Fig. 8 was used. Channels from 50 to 205 (mid-point energies from 0.3867 to 1.598 MeV) were used to estimate the concentration profile. Results are shown in Fig. 11. It is noticed that near the profile discontinuity, spurious oscillations appear and become more severe as the smoothing constraint is relaxed, i.e., λ is decreased.

While such unrealistic results near the discontinuity may appear to limit the usefulness of the LR method for samples with such discontinuous profiles, a minor modification of the LR method can greatly improve estimates of these profiles. Levenson and Coakley [21] treated such NDP cases with an adaptive Bayesian approach, wherein discontinuities were first estimated from an initial unfolding attempt, and then, using the discontinuity locations as prior information to obtain accurate estimates of the profiles. The same idea is followed here, without explicitly introducing a Bayesian model.

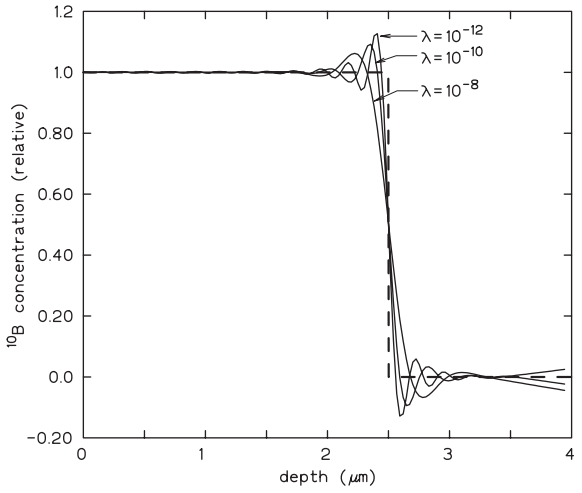

Fig. 11. Unfolded concentration profiles (solid lines) using linear regularization with linear smoothing. The actual profile used to generate the MCA spectrum is shown by the heavy dashed line. The profiles were estimated at 70 equispaced points and 156 channels of the simulated MCA energy spectrum for the α_2 ion were used.

For simplicity, we consider the case of a single discontinuity. When an LR inverted profile indicates a discontinuity as that in Fig. 11, the discontinuity location t_d is determined by inspection (or numerically by searching for inflection points, for example). Once t_d is determined, a spatial grid $t_i, i = 1, \ldots, M$, is created such that one grid point is located at the discontinuity.

A modified response matrix $\mathbf{R}$ is then constructed that explicitly incorporates the discontinuity in the numerical quadrature method used to generate $\mathbf{R}$. For example, the interval-average method of Eq. (30) is modified as follows. Eq. (29) can be written as two sums one over concentrations to the left of the discontinuity and the other over concentrations to the right, i.e.,

$$Y_i \simeq \sum_{j=1}^{d-1} \frac{c_{j+1}+c_j}{2} Q_{i,j} + \sum_{j=d}^{M-1} \frac{c_{j+1}+c_j}{2} Q_{i,j} \qquad (44)$$

where the Q_{1j} are defined by Eq. (31). If we let the concentration at t_d^- be denoted by c_d and approximate the concentration at t_d^+ by c_{d+1}, then the response matrix elements R_{ij} of Eq. (30) become

$$R_{ij} = \frac{1}{2}\begin{cases} Q_{i,1}, & j = 1 \\ Q_{i,d-1}, & j = d \\ Q_{i,d-1} + 2Q_{i,d}, & j = d+1 \\ Q_{i,j-1} + Q_{i,j}, & j = 2, \ldots, d-1, \\ & \quad d+2, \ldots, M-1 \\ Q_{i,M-1}, & j = M. \end{cases} \qquad (45)$$

The smoothing matrix $\mathbf{H}$ also is modified to prevent smoothing across the discontinuity. It can be shown that $\mathbf{H}$ becomes a two block diagonal matrix, the upper block being the smoothing matrix for all c_i up to including c_d and the lower the smoothing matrix for all $c_i, i > d$.

Results obtained with this decoupling of the profile on the two sides of the discontinuity are shown in Fig. 12. For a remarkably wide range of

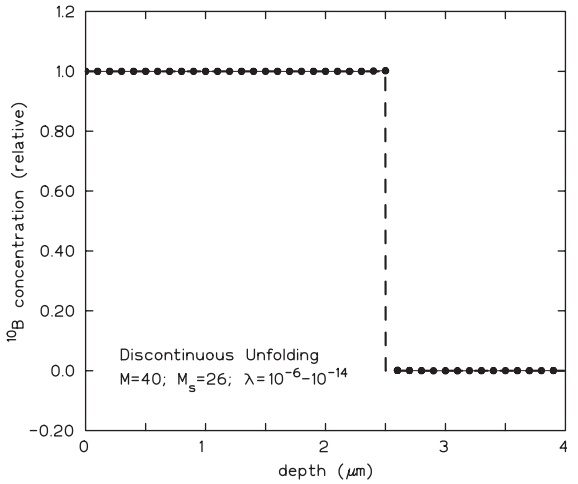

Fig. 12. Unfolded concentration profile (solid line and circles) using discontinuous linear regularization with linear smoothing. The actual profile used to generate the MCA spectrum is shown by the heavy dashed line. The profiles were estimated at 40 equispaced points and 156 channels of the simulated MCA energy spectrum for the α_2 ion were used.

the parameter λ, extremely accurate unfolded concentration profiles are obtained.

6. Conclusions

The geometric broadening of NDP energy spectra can be very pronounced for ions emerging from a sample with a curved surface. It is shown that the geometric broadening can be accounted for by using a scaled path-length distribution function provided no ions are emitted tangent to the surface and that the radius of curvature of the surface is much greater than the ion range. With this scaled path-length distribution, simulated NDP energy spectra are readily computed.

The linear regularization inversion technique for NDP spectra has been found to work remarkable well for both overdetermined and underdetermined spectral unfolding problems. For concentration profiles that have step discontinuities, a two-step unfolding procedure is proposed that first finds the discontinuities from results obtained with linear smoothing and then by using discontinuous smoothing matrices.

Acknowledgements

This work was partially funded by a DOE Nuclear Engineering Education and Research Grant DE-FG07-01ID14111.

Appendix A. Path-length calculation for curved surfaces

A.1. Equation for surfaces at depth t

Consider the two surfaces shown in Fig. 13. An outward unit normal $\hat{\mathbf{n}}(\mathbf{r},t)$ at a point $\mathbf{r}$ on the lower surface $g(\mathbf{r},t)=0$ intersects the upper surface at a corresponding point $\mathbf{r}'=\mathbf{r}+\Delta t\hat{\mathbf{n}}(\mathbf{r},t)$, a distance Δt away. First consider how the surface shape changes as the distance t from some base surface $g(\mathbf{r},0)=0$ increases. The point $\mathbf{r}'$ lies on the surface $g(\mathbf{r}',t+\Delta t)$. Thus

$$g(\mathbf{r}+\hat{\mathbf{n}}\Delta t,t+\Delta t)=g(\mathbf{r},t)=0$$

or, equivalently,

$$g(\mathbf{r},t+\Delta t)=g(\mathbf{r}-\hat{\mathbf{n}}\Delta t).$$

The right-hand side may be expanded in a first-order Taylor series (i.e., terms with $(\Delta t)^2$ and higher are neglected) to yield

$$g(\mathbf{r},t+\Delta t)\simeq g(\mathbf{r},t)-\hat{\mathbf{n}}(\mathbf{r},t)\cdot\nabla g(\mathbf{r},t).$$

By rearrangement and taking the limit as $\Delta t\to 0$ one obtains

$$\frac{\partial g(\mathbf{r},t)}{\partial t}\equiv\left[\frac{g(\mathbf{r},t+\Delta t)-g(\mathbf{r},t)}{\Delta t}\right]$$
$$=-\hat{\mathbf{n}}(\mathbf{r},t)\cdot\nabla g(\mathbf{r},t). \quad (A.1)$$

However, the unit normal $\hat{\mathbf{n}}(\mathbf{r},t)=\nabla g(\mathbf{r},t)/|\nabla g(\mathbf{r},t)|$, and Eq. (A.1) becomes

$$\frac{\partial g(\mathbf{r},t)}{\partial t}=-|\nabla g(\mathbf{r},t)|. \quad (A.2)$$

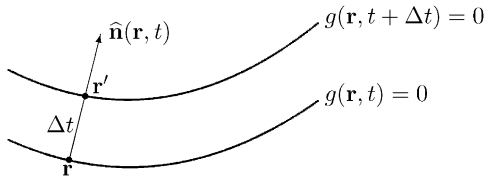

Fig. 13. Two surfaces separated by a distance Δt along the outward normal.

The solution of this equation with a specified base surface $g(\mathbf{r},0)$ then gives the surface $g(\mathbf{r},t)$ at distance t above the base surface.

A.2. Ion path length in a curved surface layer

Let $g(\mathbf{r},t)=0$ be the surface at a distance t (along the surface normal) from a base surface $g(\mathbf{r},0)=0$. An ion born at $\mathbf{r}_o$ on the base surface heads towards a detector point in the direction of the unit vector $\hat{\mathbf{p}}$ and intersects the surface $g(\mathbf{r},t)=0$ at point $\mathbf{r}(t)=\mathbf{r}_o+\hat{\mathbf{p}}s(t)$, where $s(t)$ is the straight line path travelled (see Fig. 14). As the ion travels in direction $\hat{\mathbf{p}}$ from a surface at depth t' to that at $t'+\mathrm{d}t'$, the differential path length travelled is $\mathrm{d}s(t')=\mathrm{d}t'/\cos\theta(t')$, where $\theta(t')$ is the angle between the surface normal $\hat{\mathbf{n}}(\mathbf{r},t')$ and $\hat{\mathbf{p}}$. Thus, the total path length from the base surface to the surface at t is

$$s(t)=\int_o^t \frac{\mathrm{d}t'}{\cos\theta(t')}=\int_o^t \frac{\mathrm{d}t'}{\hat{\mathbf{n}}(\mathbf{r}(t'),t')\cdot\hat{\mathbf{p}}}. \tag{A.3}$$

In NDP samples, the depths t' are very much less than the radius of curvature of the sample. Consequently, to evaluate the denominator of Eq. (A.3) a first-order Taylor's series expansion of $\hat{\mathbf{n}}(\mathbf{r},t')$ can be used, namely

$$\hat{\mathbf{n}}(\mathbf{r}(t'),t')\simeq\hat{\mathbf{n}}(\mathbf{r}_o,0)+t'\left[\frac{\partial\hat{\mathbf{n}}(\mathbf{r},t)}{\partial t}\right]_{t=t'}+\mathcal{O}(t')^2 \tag{A.4}$$

and, because $\hat{\mathbf{n}}(\mathbf{r},t')=\nabla g(\mathbf{r},t')/|\nabla g(\mathbf{r},t')|$, the denominator is thus approximated as

$$\begin{aligned}&\hat{\mathbf{p}}\cdot\hat{\mathbf{n}}(\mathbf{r}(t'),t')\\ &\simeq\hat{\mathbf{p}}\cdot\hat{\mathbf{n}}(\mathbf{r}_o,0)+t'\frac{\partial}{\partial t}\left[\frac{\hat{\mathbf{p}}\cdot\nabla g(\mathbf{r}(t),t)}{|\nabla g(\mathbf{r}(t),t)|}\right]_{t=t'}+\mathcal{O}(t')^2.\end{aligned} \tag{A.5}$$

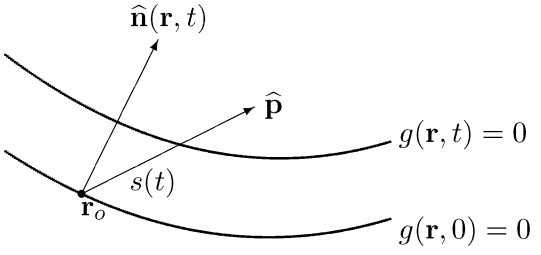

Fig. 14. The path length $s(t)$ between two surfaces travelled by an ion heading in direction $\hat{\mathbf{p}}$. Also shown in the normal $\hat{\mathbf{n}}(\mathbf{r}_o,0)$ to the base surface.

The second term in the above result involves the second derivative of the surface function $g(\mathbf{r},t)$ and is inversely proportional to the local radius of curvature R of the surface. Thus, unless the first terms vanishes, i.e., the vector $\hat{\mathbf{p}}$ is tangent to the surface so that $\hat{\mathbf{p}}\cdot\hat{\mathbf{n}}(\mathbf{r}_o,0)=0$, we can safely neglect even the first-order term. As long as the sample is collimated such that no ray joining the detector and the sample is tangent to the sample surface, the ion path length can be well approximated as

$$s(t)\simeq\int_o^t\frac{\mathrm{d}t'}{\hat{\mathbf{n}}(\mathbf{r}_o,0)\cdot\hat{\mathbf{p}}}.=\frac{t}{\cos\theta_o}. \tag{A.6}$$

References

[1] J.F. Ziegler, G.W. Cole, J.E.E. Baglin, J. Appl. Phys. 43 (1972) 3809.
[2] R.G. Downing, G.P. Lamaze, J.K. Langland, S.T. Hwang, J. Res. Natl. Inst. Stand. Technol. 98 (1993) 109.
[3] R.G. Downing, G.P. Lamaze, Semicond. Sci. Technol. 10 (1995) 1423.
[4] K.J. Coakley, R.G. Downey, G.P. Lamaze, H.C. Hoffäss, J. Biegel, C. Ronning, Nucl. Instr. and Meth. 366 (1995) 137.
[5] J.T. Maki, R.P. Fleming, D.H. Vincent, Nucl. Instr. and Meth. B 17 (1986) 147.
[6] Jandel Scientific, TableCurve, San Mataso, CA, 1996.
[7] J.K. Shultis, Notes on Neutron Depth Profiling, Report 298, Engineering Experiment Station, Kansas State University, December 2003, 41 pp.
[8] J.K. Shultis, F. Khan, B. Letellier, R.E. Faw, Appl. Radiat. Isotopes 54 (2001) 565.
[9] W.H. Press, S.A. Teukolsky, W.T. Vetterling, B.P. Flannery, Numerical Recipes, 2nd Edition, Cambridge University Press, Cambridge, 1992.
[10] J.F. Ziegler, J.P. Biersack, SRIM-2000.40, Stopping and Range of Ions in Matter, 2002; available at http://www.srim.org.
[11] S. Hoffman, in: D. Briggs, M.P. Seah (Eds.), Practical Surface Analysis by Auger and X-ray Photoelectron Spectroscopy, Wiley, New York, 1983 (Chapter 4).
[12] P.H. Van Cittert, Z. Phy. 69 (1931) 298.
[13] A.N. Tikhonov, Zh. Vych. Mat. 4 (1964) 564.
[14] A.N. Tikhonov, V.Y. Arsenin, Solutions of Ill-Posed Problems, Wiley, New York, 1977.
[15] K. Miller, SIAM J. Math. Anal. 1 (1970) 52.
[16] J. Biemond, R.L. Lagendijk, R.M. Mersereau, Proc. IEEE 78 (1990) 856.
[17] D.L. Phillips, J. Assoc. Comput. Mach. 9 (1962) 84–97.

[18] S. Twomey, J. Assoc. Comput. Mach. 10 (1963) 97–101.
[19] S. Twomey, Introduction to the Mathematics of Inversion in Remote Sensing and Indirect Measurements, Elsevier, Amsterdam, 1977.
[20] I.J. Craig, J.C. Brown, Inverse Problems in Astronomy, Adam Hilger, Bristol, UK, 1986.
[21] M.S. Levenson, K.J. Coakley, Meas. Sci. Technol. 11 (2000) 278.